Monthly Notices of the ROYAL ASTRONOMICAL SOCIETY

MNRAS **514,** 200–207 (2022) https://doi.org/10.1093/mnras/stac1343
Advance Access publication 2022 May 17

Discovery of a highly eccentric, chromospherically active binary: ASASSN-V J192114.84+624950.8

Zachary S. Way [1,2]★ T. Jayasinghe [2,3]† C. S. Kochanek,[2,3] K. Z. Stanek,[2,3] Patrick Vallely [2]‡ Todd A. Thompson [2,3] Thomas W.-S. Holoien [4]§ and Benjamin J. Shappee[5]

[1]*Department of Physics and Astronomy, Georgia State University, Atlanta, GA 30303, USA*
[2]*Department of Astronomy, The Ohio State University, 140 West 18th Avenue, Columbus, OH 43210, USA*
[3]*Center for Cosmology and AstroParticle Physics, The Ohio State University, 191 W. Woodruff Avenue, Columbus, OH 43210, USA*
[4]*The Observatories of the Carnegie Institution for Science, 813 Santa Barbara Street, Pasadena, CA 91101, USA*
[5]*Institute for Astronomy, University of Hawai'i, 2680 Woodlawn Drive, Honolulu, HI 96822, USA*

Accepted 2022 May 9. Received 2022 April 11; in original form 2021 September 15

ABSTRACT

As part of an All-Sky Automated Survey for SuperNovae (ASAS-SN) search for sources with large flux decrements, we discovered a transient where the quiescent, stellar source ASASSN-V J192114.84+624950.8 rapidly decreased in flux by $\sim$ 55 per cent ($\sim$0.9 mag) in the g band. The *Transiting Exoplanet Survey Satellite* light curve revealed that the source is a highly eccentric, eclipsing binary. Fits to the light curve using PHOEBE find the binary orbit to have $e = 0.79$, $P_{\rm orb} = 18.462$ d, and $i = 88.6^{\circ}$, and the ratios of the stellar radii and temperatures to be $R_2/R_1 = 0.71$ and $T_{\rm e,2}/T_{\rm e,1} = 0.82$. Both stars are chromospherically active, allowing us to determine their rotational periods of $P_1 = 1.52$ d and $P_2 = 1.79$ d, respectively. A Large Binocular Telescope/Multi-Object Double Spectrograph spectrum shows that the primary is a late-G- or early-K-type dwarf. Fits to the spectral energy distribution show that the luminosities and temperatures of the two stars are $L_1 = 0.48\ {\rm L}_{\odot}$, $T_1 = 5050$ K, $L_2 = 0.12\ {\rm L}_{\odot}$, and $T_2 = 4190$ K. We conclude that ASASSN-V J192114.84+624950.8 consists of two chromospherically active, rotational variable stars in a highly elliptical eclipsing orbit.

Key words: stars: chromospheres – binaries: eclipsing – stars: rotation.

1 INTRODUCTION

The All-Sky Automated Survey for SuperNovae (ASAS-SN; Shappee et al. 2014; Kochanek et al. 2017) is a survey designed to carry out unbiased searches for supernovae and other bright transient events. However, ASAS-SN simultaneously monitors the brightness of $\sim$100 million stars with $g \lesssim 18$ mag, allowing it to systematically identify and classify variable stars as well (Jayasinghe et al. 2018, 2021). Some types of variability are not automatically identified when searching for transients or normal variable stars. In particular, stars that drop suddenly and infrequently in brightness can be missed. Beginning in 2019, we began systematically searching for sources that dropped by >0.75 mag. We have reported several unusual objects with such variability, including ASASSN-V J060000.76–310027.83 (Way et al. 2019c), a likely R Coronae Borealis (RCB) variable (Way et al. 2019b), and a star with deep, dimming episodes that does not appear to be an RCB candidate (Way et al. 2019a).

One class of variable stars that is often missed by automated light-curve searches is eclipsing binaries with long periods or very short eclipses. Two ASAS-SN examples of the former are an eclipsing giant star with a 750-d orbit (Jayasinghe et al. 2020) and a giant star eclipsing binary with a 12-yr orbit (Way et al. 2021). Here, we discuss an interesting example of the latter. ASASSN-V J192114.84+624950.8 (J1921 hereafter) is a binary consisting of two chromospherically active, rotational variable stars in a highly eccentric, 18-d orbit where the eclipses span only $\sim$ 2 per cent of the total phase.

J1921 was discovered as a $\Delta g = 0.88$ mag dimming event on UT 2019-06-05.36, along with an earlier, unflagged event on UT 2016-06-29.55 that also corresponds to the primary eclipse. Fortunately, J1921 also lies close to the *Transiting Exoplanet Survey Satellite* (*TESS*; Ricker et al. 2015) continuous viewing zone, providing a densely sampled light curve that fully samples the primary and secondary eclipses.

We also detect two additional periodic signals in the *TESS* light curve at $P \sim 1.79$ d and $P \sim 1.52$ d. We attribute these to the rotation of the primary and secondary stars. Rapidly rotating main-sequence stars are generally assumed to be young (Kraft 1967). However, if the star is in a binary, the rapid rotation could be due to young age or a rotation period synchronized with the binary's orbit (Simonian, Pinsonneault & Terndrup 2019). J1921's rotational periods are not synchronized with the orbital period, so we conclude that the rapid rotation is due to the star's young age.

The two stars can be classified as either RS Canum Venaticorum (RS CVn) or BY Draconis (BY Dra) type variables. The Variable Stars Index (Watson, Henden & Price 2006) lists the requirements for an RS-CVn-type variable as (1) binary components that are of late F to late K spectral type (usually giants), (2) the presence of strong Ca II

★ E-mail: zway1@student.gsu.edu
† Ohio State Presidential Fellow.
‡ NSF Graduate Fellow.
§ NHFP Einstein Fellow.

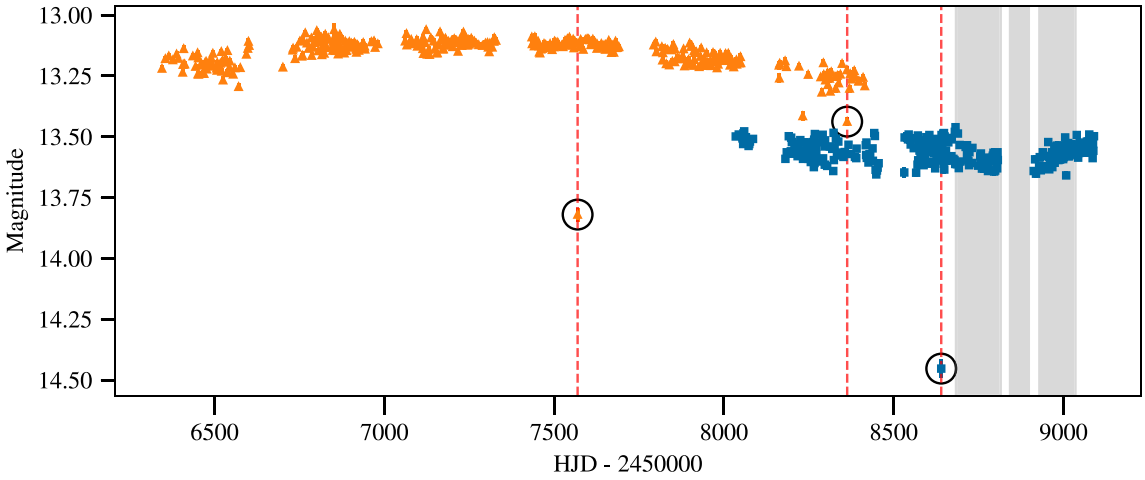

Figure 1. The ASAS-SN *g*-band (blue) and *V*-band (orange) light curves. The circled points represent the epochs that this star was dimmer than usual and they coincide with predicted eclipse times. The most recent example triggered our investigation. The primary eclipse times that coincided with ASAS-SN epochs are shown as red dashed lines. The grey stripes are the epochs spanned by *TESS* data.

H and K emission lines, (3) the presence of radio and X-ray emission, and (4) a sinusoidal light curve outside the eclipses. The criteria for BY-Dra-type variable stars exclude indicators of chromospheric activity, where the only requirements are that they are emission-line dwarfs (dKe–dMe spectral type) and have quasi-periodic light changes with periods from a fraction of a day to 120 d and amplitudes from several hundredths to 0.5 mag in *V*. In the first *Catalog of Chromospherically Active Binaries* (Strassmeier et al. 1988), they note that the difference between these two variable types is 'useful mainly from a historical viewpoint' as many chromospherically active stars can be classified as either type. We will show that J1921 satisfies the criteria for chromospheric activity and the rotational variable types listed above.

This system may be helpful in solving the outstanding discrepancy between model M-dwarf radii and direct observations (Torres & Ribas 2002; Morrell & Naylor 2019). M-dwarf model radii have been compared to observed radii in four ways. The first is through double-lined eclipsing binary systems (e.g. Mann et al. 2019). However, there are concerns that binary systems may not be representative of all M-dwarfs because tidal interactions may alter the stellar structure and inflate the star (Kraus et al. 2011). The second method is by directly measuring the radii using interferometry (see Boyajian et al. 2012). The third method uses model M-star spectra and broad-band photometry (Mann et al. 2015). Lastly, one can use *Gaia* to empirically derive a relationship between mass, luminosity, and radius (Morrell & Naylor 2019).

We show in this paper that J1921 is composed of two dwarf stars, a late-G/early-K primary and a dim, M-dwarf secondary. The orbital period lies above the cut-off for binary circularization, suggesting that the stellar components are not tidally interacting so as to synchronize the stars' rotation with their orbit (Mayor & Mermilliod 1984; Kraus et al. 2011). Each star should then be evolving as if it were a single star. Because our data are limited, we do not provide a complete solution to the binary's parameters (i.e. masses) but a more thorough analysis would provide a highly constrained model of this system. This would lend itself to comparisons to current stellar models of M-dwarfs in a similar way to Torres & Ribas (2002).

We discuss our observations in Section 2. We perform a frequency analysis of the ASAS-SN and *TESS* light curves in Section 3. We use its spectrum and spectral energy ditribution (SED) to characterize the primary star in Section 4. In Section 5, we use PHysics Of Eclipsing BinariEs (PHOEBE; Conroy et al. 2020) to model the orbit and the ratios of stellar parameters. We end with a brief summary in Section 6. Throughout our analysis, we use a distance of 315 ± 2 pc from Bailer-Jones et al. (2018). The Galactic reddening in the direction of J1921 is $E(B-V) = 0.047$ mag (Schlafly & Finkbeiner 2011), but we expect most of the dust to be behind J1921 due to its proximity.

2 OBSERVATIONS

In this section, we discuss the ASAS-SN and *TESS* light curves along with a spectrum observed using the MODS instrument at the Large Binocular Telescope (LBT).

ASAS-SN is an all-sky survey composed of automated, quadruple-mounted 14-cm telescopes at five sites. Each individual telescope has a field of view of ∼4.5 deg^2, a cadence of ∼1 d, a pixel scale of 8 arcsec, and the image full width at half-maximum (FWHM) is ∼2 pixels. Here, we use data taken at the Haleakala Observatory (Hawaii) and the Cerro Tololo International Observatory (CTIO, Chile) sites. The light curve, shown in Fig. 1, was generated using ASAS-SN's image subtraction pipeline. A more complete description of ASAS-SN's instrumentation, as well as public access to its data, can be found in Kochanek et al. (2017).

The *TESS* satellite observes the sky in predetermined sectors. It has a pixel scale of 21 arcsec, FWHM of ∼40 arcsec, and a cadence of 30 min (Ricker et al. 2015). The *TESS* light curve, shown in Fig. 2, was produced using an image subtraction pipeline modelled after ASAS-SN's. This pipeline is discussed in detail in section 2 of Vallely et al. (2021). Because the *TESS* pixels are so large, crowding may be an issue. The nearest stars to J1921 are 16.8 and 22.0 arcsec away (Bailer-Jones et al. 2018). These sources have respective *Gaia* magnitudes $G = 15.8$ mag and $G = 19.6$ mag. We discuss possible confounding effects of the former star in Section 3 but the latter is too dim to matter in this paper. We do not see any flaring activity for J1921 in either the *TESS* or ASAS-SN light curves.

Lastly, we obtained a spectrum of ASASSN-V J192114.84+624950.8 on 2019 December 21 using the Multi-Object Double Spectrographs (MODS) mounted on the twin 8.4m LBT (Pogge et al. 2010). This spectrum was reduced using a

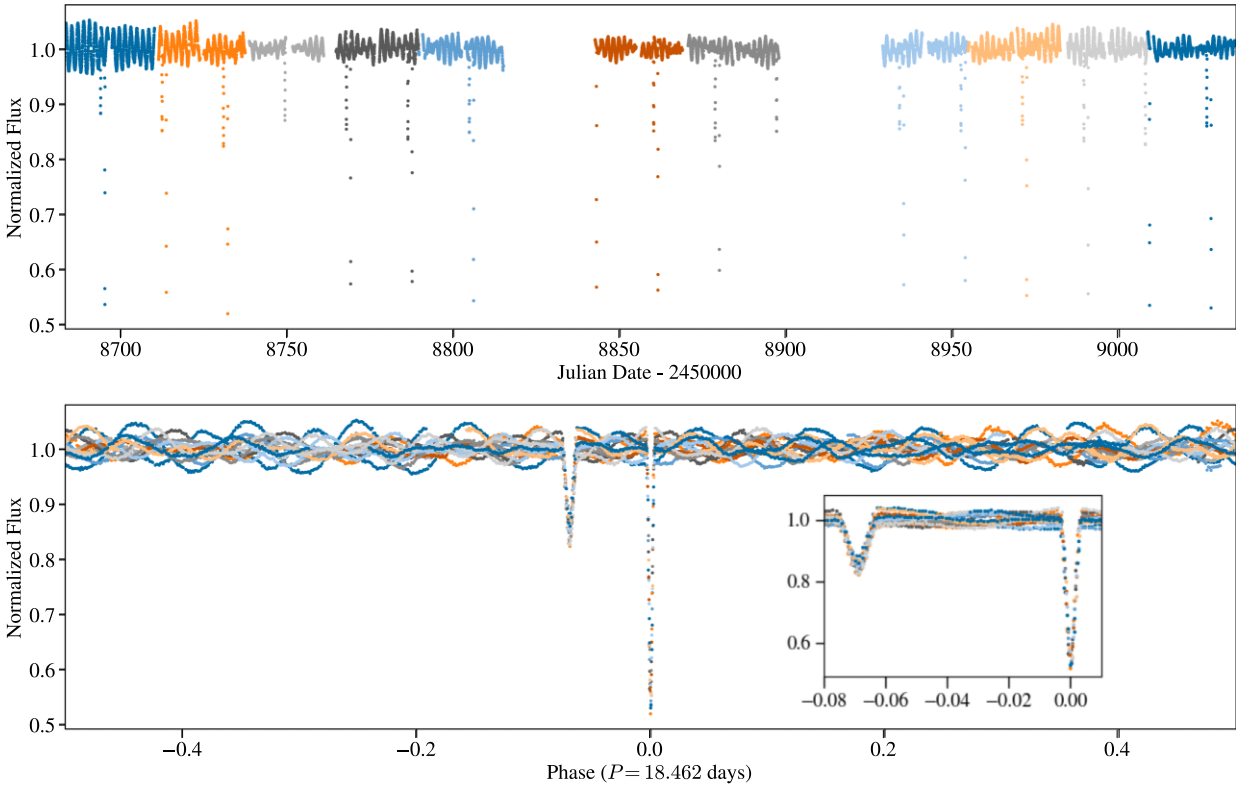

Figure 2. *Top panel*: The normalized *TESS* light curve. *Bottom panel*: The light curve folded over the orbital phase with a window showing the eclipses in more detail.

standard combination of the MODSCCDRED[1] PYTHON package, and the MODSIDL pipeline.[2] The data are shown in Fig. 6. The spectrum has a resolution of 0.5 Å, covers wavelengths from 3200.0 to 9844.5 Å, and has a mean signal to noise ratio of S/N = 416.

3 DISCOVERY AND LIGHT CURVES

In this section, we will analyse the general properties of the light curves observed by ASAS-SN and *TESS*. Fig. 1 shows the ASAS-SN *g*- and *V*-band light curves dating back to UT 2013-02-21.61. The eclipses captured by these data are shown using big circles, the last of which motivated us to investigate this source more thoroughly. There are two, slightly dimmed points on UT 2018-04-23.49 and UT 2018-09-01.38. The former is outside of both the primary and secondary eclipse's FWHM while the latter coincides with a primary eclipse.

A Lomb–Scargle (Scargle 1982) periodogram of the ASAS-SN *V*-band data is dominated by diurnal aliasing, causing J1921 to be rejected as a rotational variable source in Jayasinghe et al. (2018). A Lomb–Scargle periodogram of the *g*-band data shows a clear peak at ∼1.79 d that corresponds to one of the rotational signals we find below. This period was also detected by the Zwicky Transient Facility (ZTF) (Chen et al. 2020). The second rotational period at ∼1.52 d was not detected in the ground-based data. In addition to the eclipses, there is a slow, secular rise and fall in the *V*-band flux that we believe is real but do not discuss further in this paper.

Fig. 2 shows 11 sectors of *TESS* observations from UT 2019-07-18.86 to UT 2019-11-2.17 normalized so that the median flux is 1. The light curve was produced using the adaption of the ASAS-SN difference imaging pipeline for *TESS* data described in Vallely et al. (2021). Each sector's differential light curve was normalized to have a mean flux equal to the *TESS* Input Catalog source (T = 12.282 mag). The nature of the source is now clear – both primary and secondary eclipses of the eccentric orbit are seen against a baseline of quasiperiodic variability on a time scale much shorter than the orbital period.

Fig. 3 shows the Lomb–Scargle periodogram (Scargle 1982) of the *TESS* data. There are two significant peaks, with a strong signal at ∼1.79 d and a weaker one at ∼1.52 d. Fig. 4 shows the *TESS* data folded to these periods and excluding the eclipses. Our hypothesis is that these two periods are due to the rotational modulation of spots on the primary and secondary stars. There is a dim background star (G = 15.8 mag) located 16.8 arcseconds away that could account for the weaker periodic signal. We cannot claim complete certainty that the two stars in J1921 account for the two signals due to the *TESS* image FWHM of ∼40 arcsec. However, for the G = 15.8 mag star to produce an apparent 4 per cent modulation of the observed flux, its variability amplitude would have to be 50 per cent that is unusual for rotational variability.

The Lomb–Scargle method does not clearly show a signal at the orbital period because the algorithm works poorly for systems with narrow eclipses. We instead used the box least squares algorithm (Kovács, Zucker & Mazeh 2002) to find the orbital period. We masked the out-of-eclipse data by replacing any normalized flux >0.964 with 1, leaving a flat light curve punctuated by the eclipses. This prevents the box least squares algorithm from detecting the rotational signals. The lower panel in Fig. 3 shows the resulting periodogram with a peak at the eclipsing binary period of $P_{\rm orb}$ = 18.461 99 d. Fig. 2 shows the light curve in the top panel folded

[1] http://www.astronomy.ohio-state.edu/MODS/Software/modsCCDRed/
[2] http://www.astronomy.ohio-state.edu/MODS/Software/modsIDL/

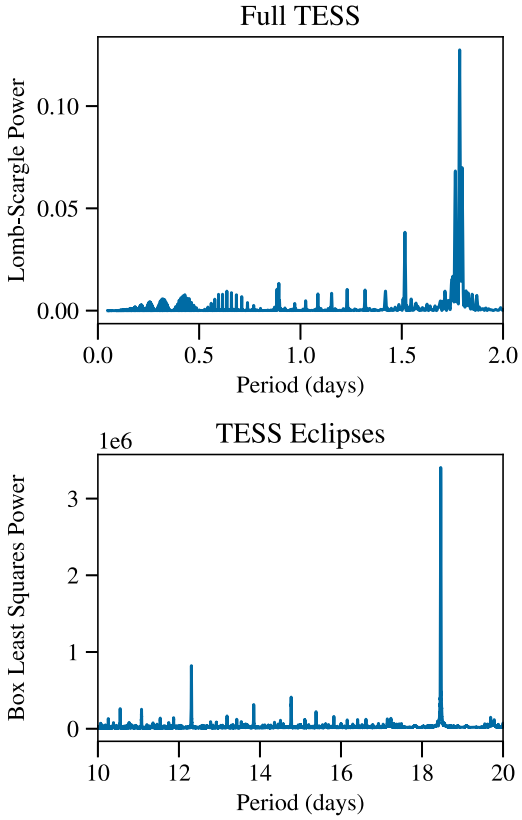

Figure 3. *Top panel:* The Lomb–Scargle periodogram for the *TESS* data shown at short periods to search for the rotational signals. *Bottom panel:* The box least square periodogram for the masked *TESS* data used to search for the longer orbital period.

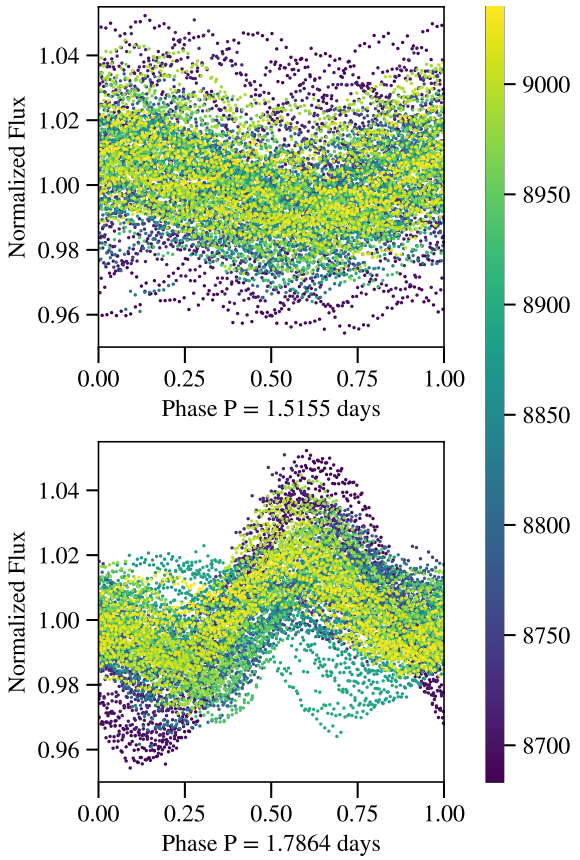

Figure 4. The *TESS* data phased to the rotation periods found in the Lomb–Scargle periodogram. The colour is coded by the epoch of the observations to show how the light curve changes with time. The eclipses have been masked.

to this period. The asymmetry of the eclipse phases means that the binary orbit is very elliptical. The eclipses at their FWHM only cover 1.05 per cent of the total phase, which explains why ASAS-SN only observed a few dimming events, even with its ∼1 d *g*-band cadence.

4 CHARACTERIZING THE PRIMARY

We can characterize the primary star by using its SED and spectrum (shown in Fig. 5 and Fig. 6, respectively). Neither should be strongly affected by the secondary because it is significantly dimmer than the primary . The spectrum is that of a late-G- or early-K-type dwarf, consistent with the temperature and luminosity reported in Gaia DR2 of 4995^{+220}_{-70} K and 0.603 ± 0.008 $L_\odot$ (Gaia Collaboration 2018).

J1921 shows evidence of strong chromospheric activity, a phenomena associated with rapid rotation and thick convection zones (Noyes et al. 1984). An exhaustive list of spectroscopic indicators of chromospheric activity can be found in section 3 of Zhang, Pi & Zhu (2015). Of these indicators, we see that the Na I D_1 and D_2, Ca II infrared triplet, and Hα absorption features are all partially filled in by emission. We also see emission peaks inside the broad Ca H and K absorption lines. Following the method laid out by Noyes et al. (1984) and Henry et al. (1996), we used the H and K lines and the APASS $B - V$ colour to find that the chromospheric emission ratio is $\log R'_{\rm HK} = -4.23$ with a measured flux index $S = 0.61$. This is indicative of very strong chromospheric activity. J1921 lies well above the minimum value for chromospheric activity ($\log R'_{\rm HK} = -4.75$) and near the -4.20 cut-off for very active stars

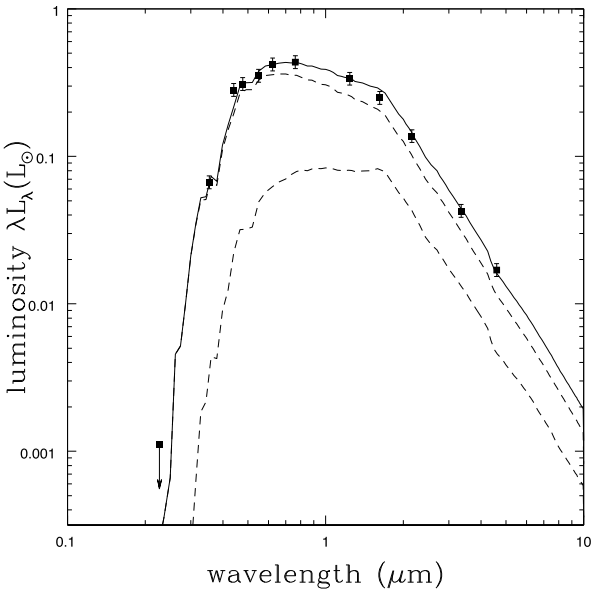

Figure 5. The SED of the system shown with models for the primary and secondary stars (dashed) and their sum (solid).

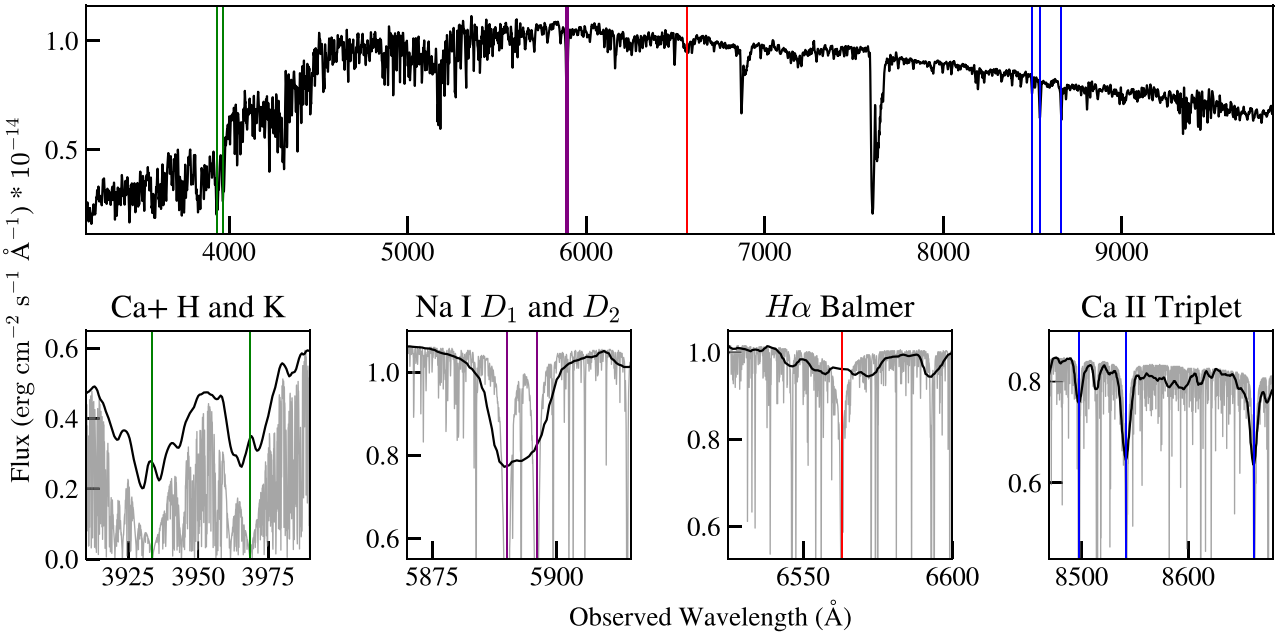

Figure 6. The LBT/MODS spectrum of J1921. Lines mark the Ca II H and K (green), Na D_1 and D_2 (purple), H α absorption (red), and the Ca II triplet (blue), which are shown in the lower panels from left to right. We superpose a BT-Settl (Allard 2014) model spectrum of a dwarf with no chromospheric activity. The model's parameters are $T_e = 5000$ K, $\log g = 4.5$, and a metallicity $Z = 0$.

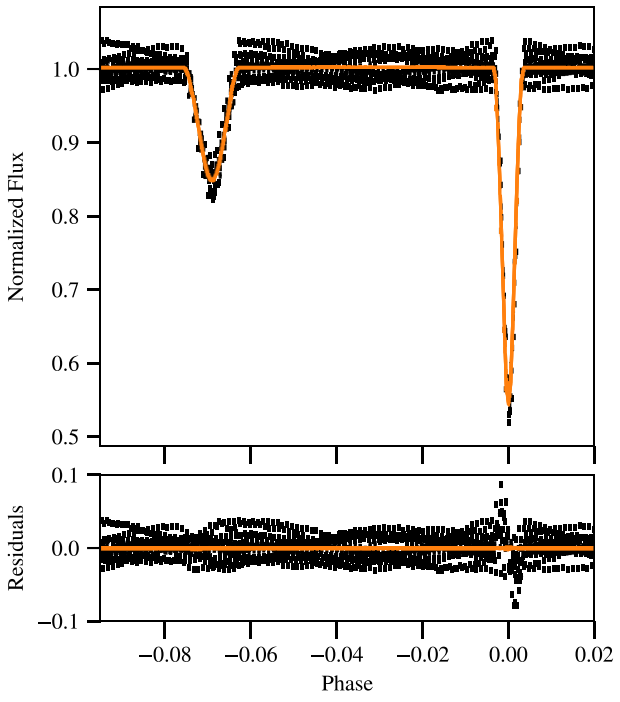

Figure 7. The top panel shows the TESS data with 100 light curves sampled within 1σ of our posterior distribution (see Fig. 8). The bottom panel shows the flux residuals. The errors of the TESS data are artificially inflated by a factor of 5 to prevent overfitting.

(see fig. 7 of Henry et al. 1996). These features are shown in the panels below the full spectrum in Fig. 6. In addition to the spectral indicators of activity, J1921 is an X-ray source (2RXS J192114.7+624951) in the second *ROSAT* survey (Boller et al. 2016). Based on the orbit and the stellar activity, we classify J1921 as a chromospherically active,

Table 1. Photometry of J1921.

Survey	Band	Mag	Uncertainty
GALEX	NUV[a]	18.7752	0.0510
SDSS	*u*	15.447	0.005
APASS	*i*'	12.540	–[b]
APASS	*r*'	12.808	0.008
APASS	*V*	13.127	0.012
APASS	*g*'	13.443	0.040
APASS	*B*	13.897	0.034
2MASS	K_s	10.806	0.019
2MASS	*H*	10.939	0.021
2MASS	*J*	11.388	0.020
WISE	*W*2	10.774	0.020
WISE	*W*1	10.753	0.023

[a]Used as an upper bound.
[b]No error was given.

rotational variable binary system. Chen et al. (2020) classified J1921 as a BY Dra variable due to its $P = 1.79$ d rotational modulation.

Table 1 lists the photometry we used to model the primary's spectral energy distribution (SED). Because the source is so bright, many standard sources of photometry are saturated. Here, we use the AllWISE catalogue (Cutri & et al. 2013), 2MASS (Cutri et al. 2003), APASS (Henden et al. 2015), and the SDSS *u* band (Alam et al. 2015). There is a GALEX (Bianchi, Shiao & Thilker 2017) NUV detection that we use as an upper limit because of the evidence for chromospheric activity.

We fit the SED with DUSTY (Ivezic & Elitzur 1997; Elitzur & Ivezić 2001) inside a Markov chain Monte Carlo (MCMC) wrapper (Adams & Kochanek 2015). We use the *Gaia* DR2 (Bailer-Jones et al. 2018) distance of 315 pc with no foreground extinction. For our stellar atmospheres, we used the models in Castelli & Kurucz (2003) and assumed minimal flux errors of 10 per cent to account for

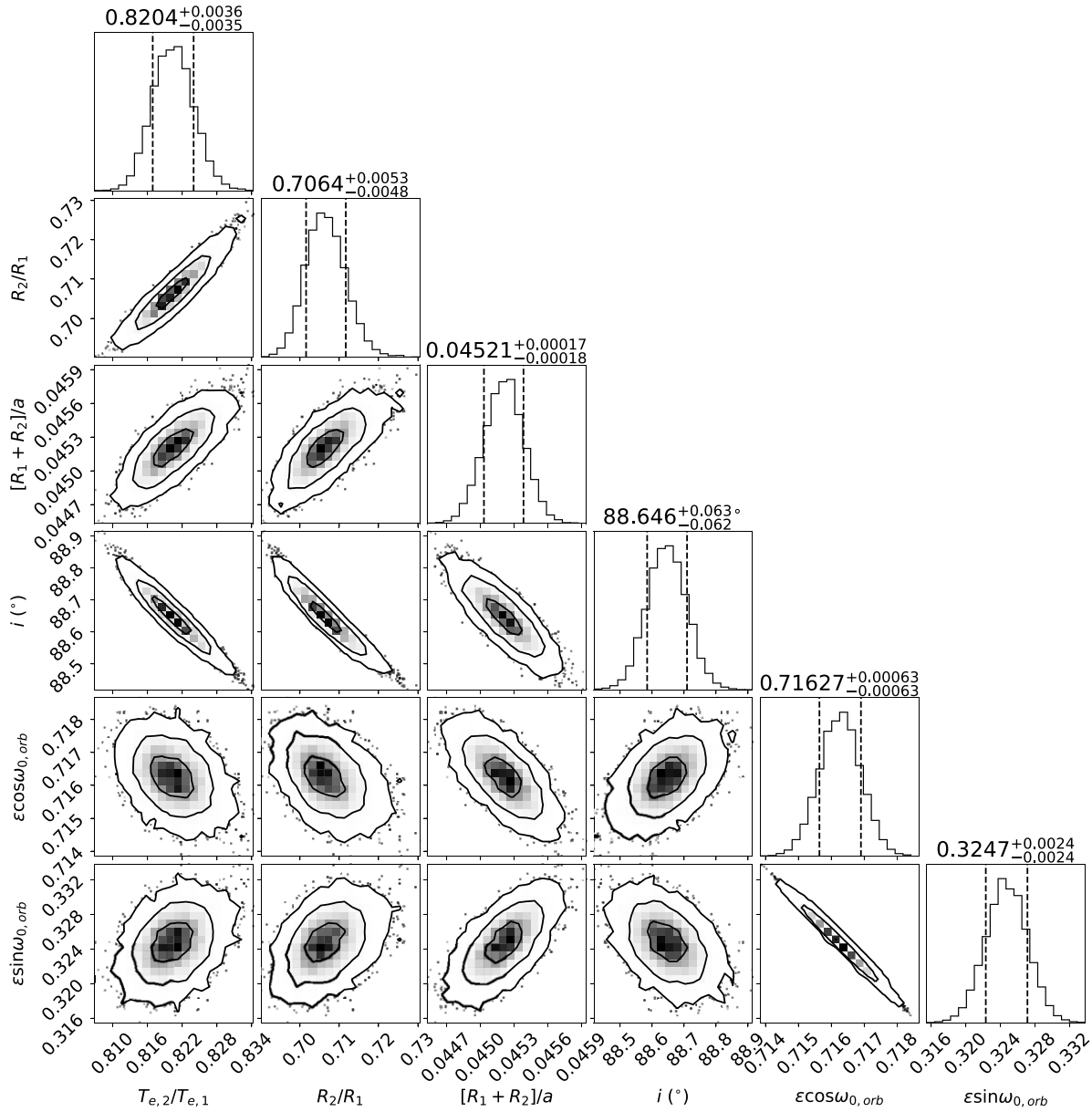

Figure 8. The posterior distribution of the binary and stellar parameters optimized in the PHOEBE fits to the *TESS* data in Section 5.

any systematic issues. This leads to a best-fitting model with $\chi^2 = 8.4$ that has a temperature of $T_e = 4930$ K and a total luminosity of $L = 0.62$ L$_\odot$. This is consistent with our spectral classification and the *Gaia* DR2 (Gaia Collaboration 2018) temperature estimate. Given the results in Section 5 for the radius and temperature ratios of the two components, we roughly modelled the SED as two stars and find that the SED is well fit by a $T_{e,1} = 5050$ K, $L_1 = 0.48$ L$_\odot$ primary combined with a $T_{e,2} = 4190$ K, $L_2 = 0.12$ L$_\odot$ secondary. The SEDs of the component stars and their sum are shown in Fig. 5.

5 ECLIPSE MODELLING

We modelled the *TESS* light curve with the PHOEBE (Prša & Zwitter 2005; Prša et al. 2016; Horvat et al. 2018; Conroy et al. 2020) PYTHON code. We use a fixed period of $P_{orb} = 18.461\,99$ d. We artificially inflate the *TESS* photometric errors by a factor of 5 because they are dominated by systematics. Even without radial velocities, we can constrain the effective temperatures, radii, eccentricity, argument of periapsis, and inclination of the system. We use the ELLC (Maxted 2016) package to model our light curves in the PHOEBE architecture.

We begin our analysis by roughly estimating the ratio of the effective temperatures. We can approximate this from the *TESS* light curve using (equation 7.11 of Carroll & Ostlie 2006)

$$\frac{B_0 - B_1}{B_0 - B_2} = \left(\frac{T_{e,2}}{T_{e,1}}\right)^4, \quad (1)$$

where B_0 is the out-of-eclipse flux, B_i are the flux minima during eclipse, and $T_{e,i}$ are the component effective temperatures. We find $T_{e,2}/T_{e,1} \sim 0.76$.

We then use PHOEBE's Gaussian eclipse model to estimate the geometry of the light curve. Using this estimate, we can approximate the eccentricity ($e \sim 0.783$) and argument of periapsis ($\omega_0 \sim$

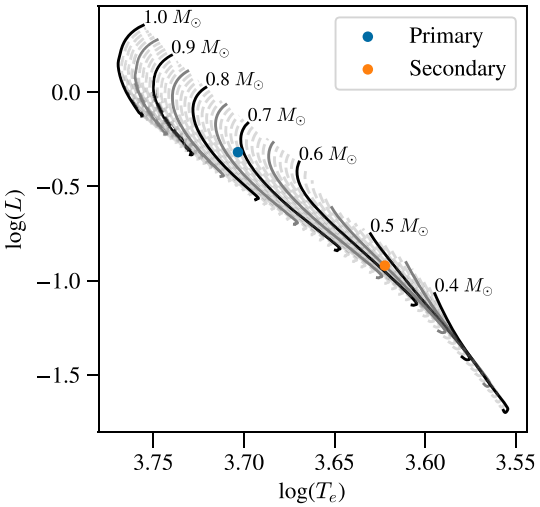

Figure 9. The primary and secondary temperatures and luminosities are shown over a range of MIST evolutionary tracks. We do not show errors here as they would be entirely systematic. The isochrones span 0.4–1 $M_\odot$ with every multiple of 0.05 $M_\odot$ shown as a solid line. The MIST models are evolved over the main sequence (from ZAMS to TAMS) with solar metallicity.

Table 2. The parameters fit in our final MCMC analysis. Variables that are ratios must be greater than zero. The posterior uncertainties are rounded to the largest significant figure.

Variable	Prior $\pm 1\sigma$	Posterior
$T_{e,2}/T_{e,1}$	0.83 ± 0.05	0.820 ± 0.004
R_2/R_1	0.73 ± 0.10	0.706 ± 0.005
$(R_1 + R_2)/a$	0.05 ± 0.10	0.0456 ± 0.0002
Inclination (i)	$88.44 \pm 0.50°$	$88.65 \pm 0.06°$
$e \cos \omega_0$	0.71 ± 0.10	0.7163 ± 0.0006
$e \sin \omega_0$	0.33 ± 0.10	0.325 ± 0.002
e[a]	–	0.7864 ± 0.0004

[a]Calculated from posterior distribution.

22.94°). Given these initial estimates, we optimized the model using the Nelder–Mead simplex algorithm (Gao & Han 2012) to estimate the ratio of effective temperatures ($T_{e,2}/T_{e,1}$), the ratio of radii (R_2/R_1), the ratio of the summed radii to the semimajor axis ($[R_1 + R_2]/a$), inclination (i), eccentricity (e), and argument of periapsis (ω_0). We keep the effective temperature ($T_{e,1}$) and radius (R_1) of the primary constrained by the single star values found in Section 4 for this optimization since these fits cannot determine either quantity.

Finally, we estimated the uncertainties using the EMCEE (Foreman-Mackey et al. 2013) MCMC package integrated into PHOEBE. Based on early fits and the SED fit at the end of Section 4, we fix $q = 0.3$, $T_{e,1} = 5050$ K, and $R_1 = 0.907$ $R_\odot$ for our analysis. We used Gaussian priors centred around the Nelder–Mead results and marginalize over, but do not directly fit, the primary's passband luminosity (L_{pb}). Fig. 7 shows 100 light curves sampled within 1σ of our posterior distribution. The full distribution is shown in Fig. 8 with the parameter values listed in the third column of Table 2. For this model, periastron would occur at phase −0.017. We do not see any obvious residual anomalies here.

Our model is incomplete until a radial velocity curve is observed. However, using the model from Section 5, we can compare the effective temperatures and radii to MESA Isochrones & Stellar Tracks (MIST) evolutionary tracks (Paxton et al. 2011, 2013, 2015; Choi et al. 2016; Dotter 2016). Fig. 9 shows a range of stellar models with solar metallicity evolving from zero-age main sequence (ZAMS) to terminal-age main sequence (TAMS). The luminosities and temperatures of the stars are consistent with masses $M_1 \sim 0.71$ $M_\odot$ and $M_2 \sim 0.55$ $M_\odot$. This is consistent with our spectral analysis in Section 4.

6 SUMMARY

During the ongoing ASAS-SN (Shappee et al. 2014; Kochanek et al. 2017) survey, we discovered the variability of ASASSN-V J192114.84+624950.8 as a $\Delta g = 0.88$ mag dip in brightness. Then, using *TESS* (Ricker et al. 2015) photometry, we found the source to be a highly eccentric, eclipsing binary with rotational variation. A Lomb–Scargle periodogram of the light curve shows the periods of rotation at $P = 1.52$ d and $P = 1.79$ d. A box least squares periodogram of the light curve, modified to mask the rotational variability, reveals the orbital period to be $P_{orb} = 18.46$ d.

In order to characterize the system, a spectrum of J1921 was taken using the MODS mounted on the twin 8.4m LBT (Pogge et al. 2010). The spectrum is that of a late-G- or early-K-type dwarf with indicators of chromospheric activity. We fit the spectral energy distribution as a sum of the two component stars and find a best-fitting model with $L_1 = 0.48$ $L_\odot$, $T_1 = 5050$ K, $L_2 = 0.12$ $L_\odot$, and $T_2 = 4190$ K.

We conclude by using PHOEBE (Prša & Zwitter 2005; Prša et al. 2016; Horvat et al. 2018; Conroy et al. 2020) and ELLC (Maxted 2016) to model the light-curve eclipses. After some optimization, we determine the errors of the orbital parameters with the EMCEE (Foreman-Mackey et al. 2013) MCMC package. We find the eccentricity and inclination to be $e = 0.79$ and $i = 88.65°$. A full list of parameters and their errors can be found in Table 2.

This system, due to its proximity and peculiar orbit, may be interesting for the studies of the discrepancy between theoretically predicted and actual radii of late-type dwarfs (Torres & Ribas 2002; Morrell & Naylor 2019). A thorough analysis of the radial velocity curve, multiband eclipse observations, and the spectroscopic properties of the stars should yield a complete solution for the masses, radii, luminosities, and temperatures of the two stars, allowing comparisons to stellar models similar to Torres & Ribas (2002) and Mann et al. (2019).

ACKNOWLEDGEMENTS

PJV was supported by the National Science Foundation Graduate Research Fellowship Program under grant no. DGE-1343012. TJ was supported by the Ohio State University Presidential Fellowship. CSK and KZS were supported by National Science Foundation (NSF) grants AST-1814440 and AST-1908570. Support for TW-SH was provided by NASA through the NASA Hubble Fellowship grant HST-HF2-51458.001-A awarded by the Space Telescope Science Institute, which is operated by the Association of Universities for Research in Astronomy, Inc., for NASA, under contract NAS5-265. BJS was supported by NSF grants AST-1907570, AST-1908952, AST-1920392, and AST-1911074.

We thank Las Cumbres Observatory and its staff for their continued support of ASAS-SN. ASAS-SN is funded in part by the Gordon and Betty Moore Foundation through grants GBMF5490 and

GBMF10501 to the Ohio State University, NSF grant AST-1908570, the Mt. Cuba Astronomical Foundation, the Center for Cosmology and AstroParticle Physics (CCAPP) at OSU, the Chinese Academy of Sciences South America Center for Astronomy (CAS-SACA), and the Villum Fonden (Denmark). Development of ASAS-SN has been supported by NSF grant AST-0908816, the Center for Cosmology and AstroParticle Physics at the Ohio State University, the Mt. Cuba Astronomical Foundation, and by George Skestos.

This paper includes data collected by the *TESS* mission, which are publicly available from the Mikulski Archive for Space Telescopes (MAST). Funding for the *TESS* mission is provided by NASA's Science Mission directorate.

The LBT is an international collaboration among institutions in the United States, Italy, and Germany. LBT Corporation partners are The Ohio State University and The Research Corporation, on behalf of The University of Notre Dame, University of Minnesota, and University of Virginia; The University of Arizona on behalf of the Arizona university system; Istituto Nazionale di Astrofisica, Italy; and LBT Beteiligungsgesellschaft, Germany, representing the Max-Planck Society, the Astrophysical Institute Potsdam, and Heidelberg University.

This publication makes use of data products from the Wide-field Infrared Survey Explorer, which is a joint project of the University of California, Los Angeles, and the Jet Propulsion Laboratory/California Institute of Technology, funded by the National Aeronautics and Space Administration.

This research has made use of the VizieR catalogue access tool, CDS, Strasbourg, France. This research also made use of ASTROPY, a community-developed core PYTHON package for astronomy (Astropy Collaboration 2018).

DATA AVAILABILITY

Except for the LBT spectrum, all data used in this paper are publicly available. The spectrum will be shared on reasonable request to the corresponding author.

REFERENCES

Adams S. M., Kochanek C. S., 2015, MNRAS, 452, 2195
Alam S. et al., 2015, ApJS, 219, 12
Allard F., 2014, in Booth M., Matthews B. C., Graham J. R., eds, Exploring the Formation and Evolution of Planetary Systems, Vol. 299. Cambridge Univ. Press, Cambridge, p. 271
Astropy Collaboration, 2018, AJ, 156, 123
Bailer-Jones C. A. L., Rybizki J., Fouesneau M., Mantelet G., Andrae R., 2018, AJ, 156, 58
Bianchi L., Shiao B., Thilker D., 2017, ApJS, 230, 24
Boller T., Freyberg M. J., Trümper J., Haberl F., Voges W., Nandra K., 2016, A&A, 588, A103
Boyajian T. S. et al., 2012, ApJ, 757, 112
Carroll B. W., Ostlie D. A., 2006, An Introduction to Modern Astrophysics and Cosmology. Pearson Addison-Wesley, San Francisco
Castelli F., Kurucz R. L., 2003, in Piskunov N., Weiss W. W., Gray D. F., eds, Modelling of Stellar Atmospheres, Vol. 210. p. Proceedings of the 210th Symposium of the International Astronomical Unionheld at Uppsala University, Uppsala, Sweden, p. A20
Chen X., Wang S., Deng L., de Grijs R., Yang M., Tian H., 2020, ApJS, 249, 18
Choi J., Dotter A., Conroy C., Cantiello M., Paxton B., Johnson B. D., 2016, ApJ, 823, 102
Conroy K. E. et al., 2020, ApJS, 250, 34
Cutri R. M. et al., 2003, The IRSA 2MASS All-Sky Point Source Catalog, NASA/IPAC Infrared Science Archive, http://irsa.ipac.caltech.edu/applications/Gator/
Cutri R. M. et al., 2013, VizieR Online Data Catalog: AllWISE Data Release (Cutri+ 2013), https://wise2.ipac.caltech.edu/docs/release/allwise/expsup/
Dotter A., 2016, ApJS, 222, 8
Elitzur M., Ivezić Ž., 2001, MNRAS, 327, 403
Foreman-Mackey D., Hogg D. W., Lang D., Goodman J., 2013, PASP, 125, 306
Gaia Collaboration, 2018, A&A, 616, A1
Gao F., Han L., 2012, Comput. Optim. Appl., 51, 259
Henden A. A., Levine S., Terrell D., Welch D. L., 2015, in American Astronomical Society Meeting Abstracts, Vol. 225. American Astronomical Society, Seattle, Washington, p. 336.16
Henry T. J., Soderblom D. R., Donahue R. A., Baliunas S. L., 1996, AJ, 111, 439
Horvat M., Conroy K. E., Pablo H., Hambleton K. M., Kochoska A., Giammarco J., Prša A., 2018, ApJS, 237, 26
Ivezic Z., Elitzur M., 1997, MNRAS, 287, 799
Jayasinghe T. et al., 2018, MNRAS, 477, 3145
Jayasinghe T. et al., 2020, Astron. Telegram, 13745, 1
Jayasinghe T. et al., 2021, MNRAS, 503, 200
Kochanek C. S. et al., 2017, PASP, 129, 104502
Kovács G., Zucker S., Mazeh T., 2002, A&A, 391, 369
Kraft R. P., 1967, ApJ, 150, 551
Kraus A. L., Tucker R. A., Thompson M. I., Craine E. R., Hillenbrand L. A., 2011, ApJ, 728, 48
Mann A. W., Feiden G. A., Gaidos E., Boyajian T., von Braun K., 2015, ApJ, 804, 64
Mann A. W. et al., 2019, ApJ, 871, 63
Maxted P. F. L., 2016, A&A, 591, A111
Mayor M., Mermilliod J. C., 1984, in Maeder A., Renzini A., eds, Observational Tests of the Stellar Evolution Theory, Vol. 105, p. International Astronomical Union Symposiumheld in Geneva, Switzerland, p. 411
Morrell S., Naylor T., 2019, MNRAS, 489, 2615
Noyes R. W., Hartmann L. W., Baliunas S. L., Duncan D. K., Vaughan A. H., 1984, ApJ, 279, 763
Paxton B., Bildsten L., Dotter A., Herwig F., Lesaffre P., Timmes F., 2011, ApJS, 192, 3
Paxton B. et al., 2013, ApJS, 208, 4
Paxton B. et al., 2015, ApJS, 220, 15
Pogge R. W. et al., 2010, in McLean I. S., Ramsay S. K., Takami H., eds, Proc. SPIE Conf. Ser. Vol. 7015, Ground-Based and Airborne Instrumentation for Astronomy III. SPIE, Bellingham, p. 77350A
Prša A., Zwitter T., 2005, ApJ, 628, 426
Prša A. et al., 2016, ApJS, 227, 29
Ricker G. R. et al., 2015, J. Astron. Telesc. Instrum. Syst., 1, 014003
Scargle J. D., 1982, ApJ, 263, 835
Schlafly E. F., Finkbeiner D. P., 2011, ApJ, 737, 103
Shappee B. J. et al., 2014, ApJ, 788, 48
Simonian G. V. A., Pinsonneault M. H., Terndrup D. M., 2019, ApJ, 871, 174
Strassmeier K. G., Hall D. S., Zeilik M., Nelson E., Eker Z., Fekel F. C., 1988, A&AS, 72, 291
Torres G., Ribas I., 2002, ApJ, 567, 1140
Vallely P. J., Kochanek C. S., Stanek K. Z., Fausnaugh M., Shappee B. J., 2021, MNRAS, 500, 5639
Watson C. L., Henden A. A., Price A., 2006, Society for Astronomical Sciences Annual Symposium, 25, 47
Way Z. et al., 2019a, Astron. Telegram, 13106, 1
Way Z. et al., 2019b, Astron. Telegram, 13159, 1
Way Z. et al., 2019c, Astron. Telegram, 13346, 1
Way Z. et al., 2021, Astron. Telegram, 14436, 1
Zhang L.-Y., Pi Q.-F., Zhu Z.-Z., 2015, Res. Astron. Astrophys., 15, 252

This paper has been typeset from a TEX/LATEX file prepared by the author.